JTTEE5 10:105-110

Modeling of Plasma Spraying of Two Powders

B. Dussoubs, A. Vardelle, G. Mariaux, N.J. Themelis, and P. Fauchais

(Submitted 27 July 1999; in revised form 19 October 2000)

The behavior of metal and ceramic powders co-sprayed through a plasma jet was simulated using a commercial fluid dynamics model in which the particles are considered as discrete Langrangian entities. Computations were carried out for the plasma jet and the injected particles using (a) a steady-state three-dimensional (3-D) jet and (b) a simplified two-dimensional (2-D) model. An analytical method was used to estimate the appropriate injection velocities for the metal and ceramic particles, injected through opposing nozzles perpendicular to the plasma flow, so that their "mean" trajectories would impinge on the same area on the target surface. Comparison of the model projections with experimental measurements showed that this method of computation can be used to predict and control the behavior of particles of widely different properties.

Keywords functionally graded materials, particle injection, particle modeling, plasma co-spraying

1. Introduction

The simultaneous spraying of metal and ceramic powders can be used to produce what is called functionally graded materials (FGM) that exhibit continuous or stepwise variations in composition and/or microstructure.[1] One of the key applications is to reduce the interface effects between coating and substrate, since co-spraying allows a gradual variation of properties. For example, this technique has proven useful in avoiding thermal expansion coefficient mismatch in thermal barrier coatings, thus limiting high stress regions and improving coating lifetime.

In plasma co-spraying, it is essential that the "splats" from the two types of particles overlap on the substrate. When using a single plasma torch system, two methods of powder injection can be used in the production of FGM.

- The two powders are mixed and fed through a single injection port; in this case, the higher density particles must be of smaller size than the lighter ones.
- The two types of particles are injected through two separate injectors. In this case, the carrier gas flow, injector-to-substrate distance, and angle between injector and plasma jet axis can be varied separately so as to obtain overlapping of splats on the substrate.

In the production of FGM by plasma co-spraying, the dispersion of particles in the jet flow and the deposition efficiency must be carefully controlled in order to produce coatings with a consistent composition. Deviations from the planned gradient occur when the different powders fed into the plasma do not impinge on the substrate at the same location, leading to inhomogeneities. Therefore, for given plasma operating conditions, it is important to understand the relationship between particle injection parameters and the resulting trajectories and temperatures. Mathematical simulation can be of great help in this matter, as will be discussed in the following sections of this paper. For the purposes of this work, the powder system iron-aluminum oxide was selected because of the range of properties offered by these two materials.

B. Dussoubs, LSG2M-ENSMN, Parc de Saurupt, 54042 Nancy, Cedex, France; **A. Vardelle, G. Mariaux,** and **P. Fauchais,** SPCTS, University of Limoges, 87060 Limoges, France; and **N.J. Themelis,** Earth and Environmental Engineering, Columbia University, New York, NY 10027. armelle@ensil.unilim.fr.

2. Mathematical Model

Computations were carried out for the plasma jet and the injected particles using (a) a steady-state three-dimensional (3-D) jet and (b) a simplified two-dimensional (2-D) model.

2.1 Modeling of 3-D Plasma Jet

The model of the plasma jet issuing in air and impinging normally on a flat substrate is based on the following assumptions:[2]

- steady-state plasma jet flow (*i.e.*, neglecting the effect of the arc movement within the nozzle);
- turbulent flow except in the potential core and close to the walls (*i.e.*, front surface of the gun, injectors, and target surface);
- plasma in local thermodynamic equilibrium and optically thin;

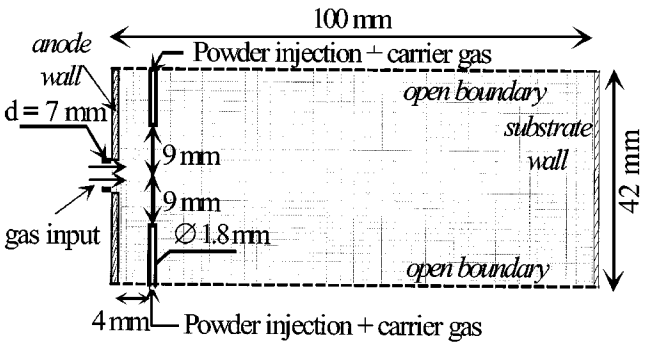

Fig. 1 Calculation domain

- no chemical reaction in the gas phase;
- multicomponent flow consisting of the plasma-forming gas, powder carrier gas, and ambient gas; and
- target surface kept at a constant temperature.

The governing equations of the gas flow (continuity equation for each component of the mixture, Navier-Stokes equations, and energy conservation equation for multicomponent gas system) are solved using the commercial code, ESTET 3.2.[3] This code is a 3-D computational fluid dynamics package simulating transient or steady, compressible, turbulent, and multicomponent reactive flow. Turbulence is modeled by the the *k*-ε model with the correction of Launder and Sharma, for low Reynolds numbers.[4] The thermodynamic and transport properties of the gas mixture are calculated using the laws of mixtures and the data of pure gases.[5] Figure 1 shows the computation domain, the boundary conditions, and the computational mesh.

The profiles of gas velocity and temperature at the nozzle exit are imposed as[6]

$$v = v_{\max} * \left(1 - \left(\frac{r}{R}\right)^2\right) \qquad \text{(Eq 1)}$$

$$T = \left(T_{\max} - T_{m,\mathrm{Cu}}\right) * \left(1 - \left(\frac{r}{R}\right)^{4.5}\right) + T_{m,\mathrm{Cu}} \qquad \text{(Eq 2)}$$

where $v_{\max}$ and $T_{\max}$ are the velocity and temperature of the plasma jet on the torch axis, T_m,Cu the melting point of copper, and R the nozzle radius; $v_{\max}$ and $T_{\max}$ are determined from the plasma-forming gas mass flow rate and the net power input to the gun.

The conservation equations for the mean values of turbulent flow, turbulent energy, and its rate of dissipation are expressed by Eq 3. Table 1 shows the transport coefficients and the source terms for all variables involved in these calculations.

$$\mathrm{div}\left(\rho\varphi\mathbf{v}\right) = \mathrm{div}\left(\Gamma_\varphi\ \mathbf{grad}\ \varphi\right) = \mathrm{S}_\varphi \qquad \text{(Eq 3)}$$

2.2 Modeling of 2-D Plasma Jet

The 2-D steady-state model is based on the same assumptions as the 3-D model. In addition, the jet flow is assumed to have azimuthal symmetry and the governing equations are written in cylindrical-polar coordinates. The effect of the carrier gas flow on the plasma jet cannot be taken into account in the 2-D model. However, earlier experiments and mathematical simulations have shown that this effect is negligible for the spray parameters of this study, where the powder is injected externally to the gun and the carrier gas flow rate is less than 10% of the plasma-forming gas flow rate.[7]

2.3 Modeling of Particle Dynamics and Heating

The acceleration and heating of particles are calculated with a Lagrangian scheme under the following assumptions:[8–10]

Table 1 Transport coefficients and source terms for the equations of the flow

φ	Γ_φ	Σ_φ
1	0	$\mathrm{div}\ (\rho\mathbf{v})$
u	$\mu_{\mathrm{eff}} = \mu + \mu_t$	$-\frac{\partial p}{\partial x} + \rho f_{\mathrm{x}} + \mathrm{div}\left(\mu_{eff}\frac{\partial v}{\partial x}\right) + \frac{\partial}{\partial x}\left(-\frac{2}{3}\mu_{eff}\ \mathrm{div}\ \mathbf{v}\right) - \frac{2}{3}\frac{\partial}{\partial x}(\rho k)$
v	μ_{eff}	$-\frac{\partial p}{\partial y} + \rho f_y + \mathrm{div}\left(\mu_{eff}\frac{\partial v}{\partial y}\right) + \frac{\partial}{\partial y}\left(-\frac{2}{3}\mu_{eff}\ \mathrm{div}\ \mathbf{v}\right) - \frac{2}{3}\frac{\partial}{\partial y}(\rho k)$
w	μ_{eff}	$-\frac{\partial p}{\partial z} + \rho f_z + \mathrm{div}\left(\mu_{eff}\frac{\partial v}{\partial z}\right) + \frac{\partial}{\partial z}\left(-\frac{2}{3}\mu_{eff}\ \mathrm{div}\ \mathbf{v}\right) - \frac{2}{3}\frac{\partial}{\partial z}(\rho k)$
H	$\rho(\kappa / C_{\mathrm{P}} \cdot \rho) + \mu_t / \mathrm{Pr}_t$	$S_H + \mathbf{v} \cdot \mathrm{grad}\ p$
X_i	$\rho \cdot D_i + \mu_t / \mathrm{Sc}_t$	0
k	$\mu + \mu_t / \sigma_k$	$-\frac{2}{3}\rho k\ \mathrm{div}\ \mathbf{v} - \frac{2}{3}\mu_t\ (\mathrm{div}\ \mathbf{v})^2 + G + \rho(G_k - \varepsilon)$
ε	$\mu + \mu_t / \sigma_\varepsilon$	$-\frac{2}{3}C_{\varepsilon_1}\rho\varepsilon\ \mathrm{div}\ \mathbf{v} - \frac{2}{3}\mu_t C_{\varepsilon_1}\frac{\varepsilon}{k}\left(\mathrm{div}\ \mathbf{v}\right)^2 + \rho\frac{\varepsilon}{k}\left(C_{\varepsilon_1}G_k - C_{\varepsilon_2}\varepsilon\right) + \frac{\varepsilon}{k}C_{\varepsilon_1}C_{\varepsilon_3}G$

with

$$G_k = \frac{\mu_t}{\rho}\left[2\left(\frac{\partial u}{\partial x}\right)^2 + 2\left(\frac{\partial v}{\partial y}\right)^2 + 2\left(\frac{\partial w}{\partial z}\right)^2 + \left(\frac{\partial u}{\partial y} + \frac{\partial v}{\partial x}\right)^2 + \left(\frac{\partial u}{\partial z} + \frac{\partial w}{\partial x}\right)^2 + \left(\frac{\partial v}{\partial z} + \frac{\partial w}{\partial y}\right)^2\right]$$

$$G = \frac{1}{\rho}\frac{\mu_t}{\sigma_k}\frac{\partial \rho}{\partial x_i}\rho f_i$$

and $$\mu_t = \rho C_\mu \frac{k^2}{\varepsilon}$$

- spherical particles,
- no interactions between particles,
- possible interactions with the walls present in the domain,
- turbulent dispersion of particles,
- lumped capacitance method for particle heating, and
- modification of plasma-particle transfer coefficients to account for the variation of gas properties in the boundary layer and particle evaporation.

The particle size distributions were in the commercially used range and 8 to 12 classes of particle sizes were used in the computation. About 2500 particle trajectories were calculated for each run. The distributions of particle velocity and position at the injector exit were obtained from an earlier calculation of gas-particle interactions inside a part of the piping system and the injector. Since the trajectories of particles in the jet flow are, to a great extent, conditioned by the injection conditions of the powder, the model must represent the latter in a realistic way. The energy balance on a particle of mass m_p yields

$$m_P \frac{dv_P}{dt} = -C_D \pi \frac{d_P^2}{4} \rho_\infty \frac{|\mathbf{v}_P - \mathbf{v}_\infty|(\mathbf{v}_P - \mathbf{v}_\infty)}{2} + m_P \mathbf{g} \qquad \text{(Eq 4)}$$

Integrating Eq 4 twice provides the position vector of the particle as a function of time. The correlation of Lee *et al.*[11] was chosen to correct the value of the drag coefficient C_D for thermal gradients in the boundary layer around the particle. In computing the dispersion of particles due to turbulence, it is necessary to "re-create" their instantaneous velocities from the mean values of the flow field. This is done by using the Csanady equations.[12–14]

As the particles are heated, they are subjected to the following sequence:

- *Heating of solid particle*

$$Q_n = h\pi d_P^2 (T_\infty - T_P) - \varepsilon_R \sigma \pi d_P^2 \left(T_P^4 - T_a^4\right) = m_P C_{P_P} \frac{dT_P}{dt} \qquad \text{(Eq 5)}$$

- *Melting at constant temperature*

The net amount of heat received by the particle from the plasma is converted to latent heat of fusion:

$$Q_n = \frac{dX_P}{dt} \frac{\pi d_P^3 \Delta H_M \rho_P}{6} \qquad \text{(Eq 6)}$$

where X_p is the molten mass fraction of the particle.

- *Heating of liquid particle and evaporation*

$$Q_n = h\pi d_P^2 (T_\infty - T_P) - \varepsilon_R \sigma \pi d_P^2 \left(T_P^4 - T_a^4\right) = m_P C_{P_P} \frac{dT_P}{dt} + \pi d_P^2 N_{vap} \Delta H_{vap} \qquad \text{(Eq 7)}$$

In this stage, the particle diameter decreases proportionally with the last term of the above equation. The heat-transfer coefficient in the above equations is calculated from the Nusselt number, Nu, using the correction of Lee *et al.*[11] The value of N_{vap}, the mass flux of vapor escaping from the particle surface, is determined from the equation proposed by Yoshida.[15]

Table of Symbols

C_D	drag coefficient
C_P	specific heat, J/kg K
d	diameter, m
F_D	drag force, kg m/s^2
f	body force, kg m/s^2
g	gravity vector, m/s^2
h	heat-transfer coefficient, W/m^2 K
H	specific enthalpy, J/kg
k	kinetic turbulent energy, m^2/s^2
m	mass, kg
N	mass flux, kg/m^2 s
OM	position vector, m
p	pressure, Pa
Q_n, $Q_{\dot{n}}$	rate of heat transfer, W
r	radius, m
R	radius of the powder injector, m
S	source term for the equations of conservation
T	temperature, K
V	velocity vector, m/s, of components u, v, and w in the Cartesian frame (x, y, z)
X	mass fraction

Greek Symbols

ε	rate of dissipation of turbulent energy, m^2/s^3
ε_R	total emissivity
φ	variable
ΔH	heat of reaction, J/kg
Γ	transport coefficient, kg/m s
κ	thermal conductivity, W/m K
μ	dynamic viscosity, kg/m s
ρ	density, kg/m^3
σ	Stefan-Boltzmann's constant, W/m^2 K^4

Subscripts

a	ambient temperature
B	boiling
eff	effective
g	gas
max	maximum
m,Cu	melting of copper
p	particle
vap	vaporization

4. Results and Discussion

4.1 Plasma Spraying Conditions

The spraying parameters used as input data for the model are shown in Table 2 and the characteristics of the feedstock mate-

Table 2 Plasma spray parameters

Gun nozzle exit	7 mm
Plasma-forming gas	45 slm Ar + 15 slm H_2
Gas mass flow rate	1.25 10^{-3} kg s^{-1}
Arc current	600 A
Effective power	21.5 kW
Stand-off distance	100 mm

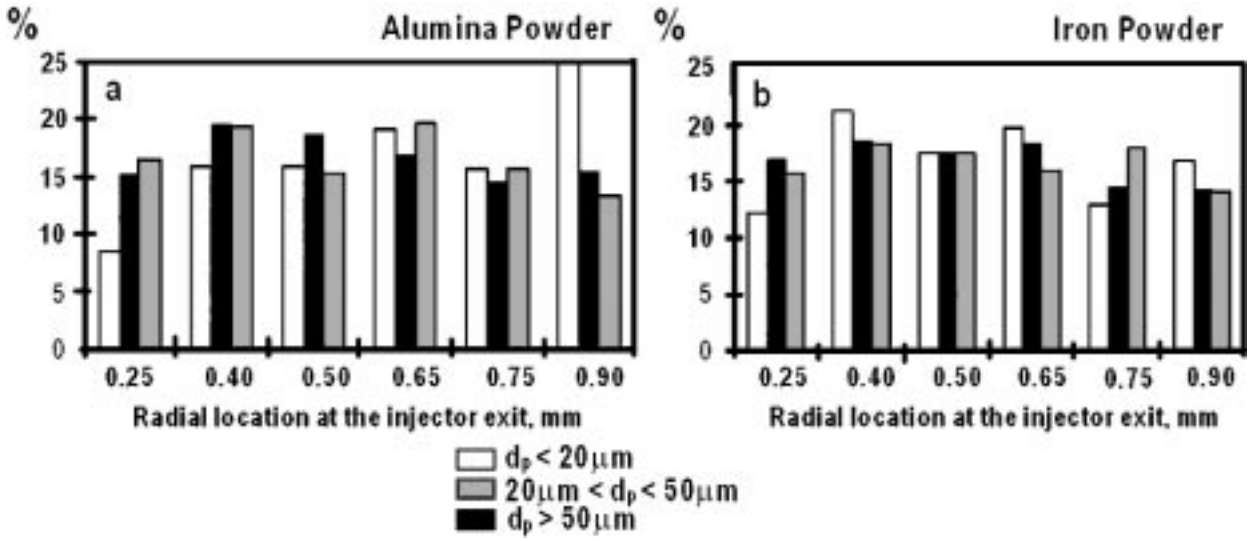

Fig. 2 Radial particle distribution at the exit of the injector: (**a**) alumina powder and (**b**) iron powder

Table 3 Powder characteristics

Material	Alumina	Iron
Melting point	2326 K	1810 K
Boiling point	3800 K	3023 K
Mass density	3900 kg m^{-3}	7800 kg m^{-3}
Specific heat (300 K)	1363 J kg^{-1} K^{-1}	600 J kg^{-1} K^{-1}
Thermal conductivity (300 K)	5 W m^{-1} K^{-1}	35 W m^{-1} K^{-1}
Particle size	10–55 μm	22–45 μm
Powder feed rate	15 g min^{-1}	15 g min^{-1}

rials in Table 3. The plasma jet issued in air at atmospheric pressure. The two powders were injected through 1.8 mm diameter ports located at 4 mm downstream of the nozzle exit and 9 mm off the jet centerline.

The simulation of the pneumatic transport of powder in the injector showed that the velocity and location of the iron particles at the injector exit depend very little on the particle size of the iron particles. The same effect was predicted for the alumina particles, except for the lightest ones of diameter less than 20 μm. The latter were more subjected to turbulent dispersion and collisions with the tube wall; about 25% of these finer particles were close to the wall and exhibited a low velocity,[16] as shown in Fig. 2. This figure shows the radial distribution of the particles at the injector exit whose radius is 0.9 mm. Position zero corresponds to the injector centerline and position 0.9 to the injector wall. Three particle size groups have been considered for alumina and iron powders: <20 μm, 20 to 50 μm, and >50 μm, the total powder percentage for each of the three particle groups being equal to 100%.

The profiles of particle and gas velocity at the injector exit were practically identical, the velocity of the iron particles being lower than that of alumina particles, as expected.

4.2 Comparison with Measurements

For alumina particles that attained temperatures above 1800 K, the model predictions for the radial distribution of particle number density, at 100 mm from the nozzle exit, were found to be in good agreement with experimental measurements,[17,18] as shown in Fig. 3. This temperature corresponded to the low limit of detection of the experimental device used to measure particle number densities from their thermal radiation.

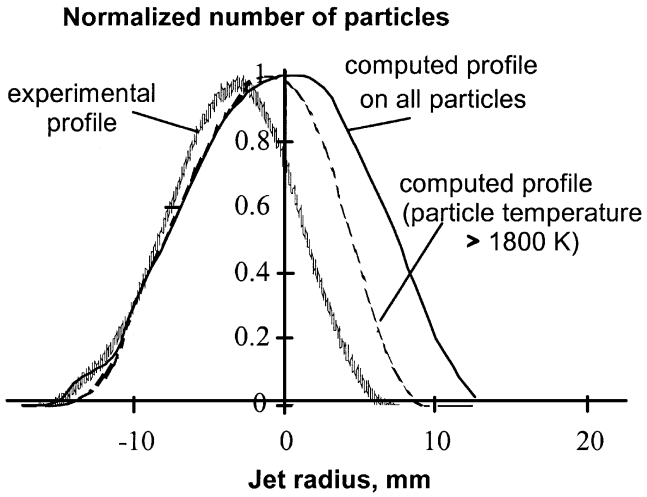

Fig. 3 Comparison of calculated and measured particle jet spreads at a location of 100 mm downstream of the nozzle exit

4.3 Co-Spraying of Alumina and Iron Powders

Using a Single Injector. In this case, the alumina and iron powders were assumed to be mixed in the powder feed line and injected in the plasma jet through a single injector normal to the jet axis (Fig. 1). The carrier gas flow rate of argon was equal to 4 slm. As shown in Fig. 4, this ensured that the distribution of the alumina particles was nearly symmetrical about the jet centerline at the substrate location. However, the alumina and iron spray spots on the substrate did not overlap completely, as the heavier iron particles penetrated deeper the plasma jet due to their higher momentum at the injection point.

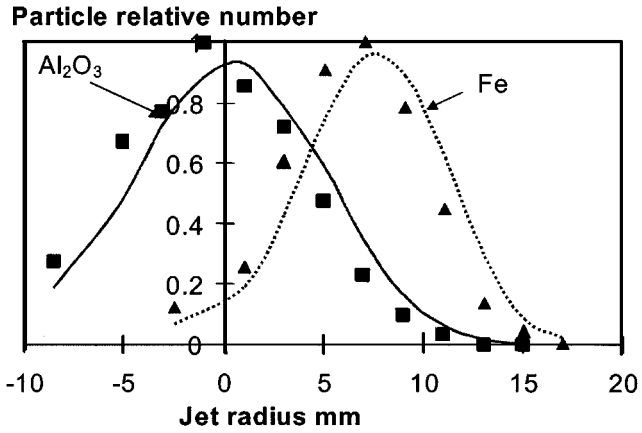

Fig. 4 Distribution of particle number vs vertical distance when alumina and iron powders injected through one injector

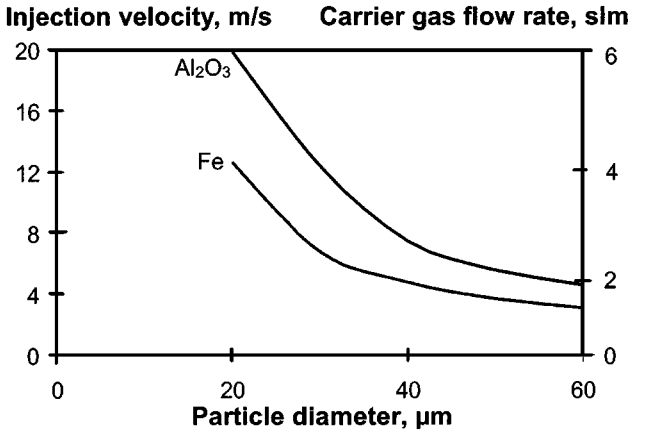

Fig. 5 Particle injection velocity and carrier gas flow rate as a function of particle size for alumina and iron powders under the spray parameters of the study

As noted earlier, when using a single common injector, the only way to provide for better overlapping of the ceramic and metal particle impingement spots on the substrate is by using a finer iron powder. However, this may result in overheating of the metal powder and a corresponding increase in particle evaporation or oxidation.

Powder Injection Using Two Diametrically Opposed Injectors. In this case, it was assumed that the alumina and iron powders were injected through two injectors normal to the jet centerline and diametrically opposed. Thus, the mixing of powders occurred within the plasma jet.

To reduce the number of numerical experiments, a 2-D analytical model was used to determine the injection velocity that would provide for iron and alumina particles of specific sizes to "land" on the substrate surface at the jet centerline.[7] The controlling kinetic energy balance is obtained by equating the rate of change of momentum of the particles to the drag force F_d in their direction of motion, *i.e.*, in the direction *y*, which is perpendicular to the jet flow (direction *x*):

$$\frac{d(m_p v_p)}{dt} = F_d \qquad \text{(Eq 8)}$$

where m_p is the mass of a particle, v_p its velocity, and F_d the drag force acting on the particle. For the Stokes region and a quasi-spherical particle,

$$F_d = 3\pi d_p v_p \mu \qquad \text{(Eq 9)}$$

By substituting in the energy balance equation (Eq 8) and integrating from time $t = 0$ (entry to jet cone) to t, under the assumption that gas viscosity is constant, the following equation is obtained:

$$\frac{v_t}{v_0} = e^{-\frac{18\mu t}{\rho_p d_p^2}} \qquad \text{(Eq 10)}$$

This equation shows that the velocity of the injected particles across the jet cone (direction *y*) decreases exponentially with time of travel. The power exponent is the dimensionless time of travel; the grouping

$$\frac{\rho_p d_p^2}{18\mu} \qquad \text{(Eq 11)}$$

is a reference time characteristic of the particles/plasma system.

The total time of flight of the particle in the horizontal direction is determined by the distribution of jet velocity within the cone envelope and by the above "reference time" group. The distance traveled by the particles in the direction *y* is related to time *t* by integrating Eq 10:

$$y = v_0 \frac{\rho_p d_p^2}{18\mu_g}\left(1 - e^{-\frac{18\mu t}{\rho_p d_p^2}}\right) \qquad \text{(Eq 12)}$$

By arbitrarily setting the radial distance *y* to be traveled by all particles at 10 mm and using Eq 12 and the computed residence time, the required injection velocity, v_0, can be calculated for each material and average particle size, so that all particles "land" on the same area on the substrate (Fig. 5). The corresponding carrier gas volume flow rate is then calculated as the product of this injection velocity and the cross-sectional area of the injector. This simplified calculation resulted in a computed carrier gas flow rate of 2.5 slm for the 35 µm iron particle, *i.e.*, the average size of particle distribution, in comparison to the 4 slm flow rate used for the alumina powder. Figure 6 shows the predicted distribution of particle number density at the substrate location.

As would be expected, the computations also showed that the finest particles did not travel as far in the radial direction as the larger ones. This effect was less marked for the heavier iron particles. It is interesting to note that for the plasma co-spraying of zirconia and NiCrAlY, Smith *et al.*[1] injected the ceramic powder, through an injector 90° to the plasma jet and located below the horizontal torch axis, while the metal powder injector was located above the torch axis and at an angle of 105°. Numerical simulation using the same injector configuration for the plasma powder system of this study resulted in good overlapping of both particle spray spots on the substrate, when carrier gas flows of 4 slm for alumina and 1.5 slm for iron were used. In this case, the

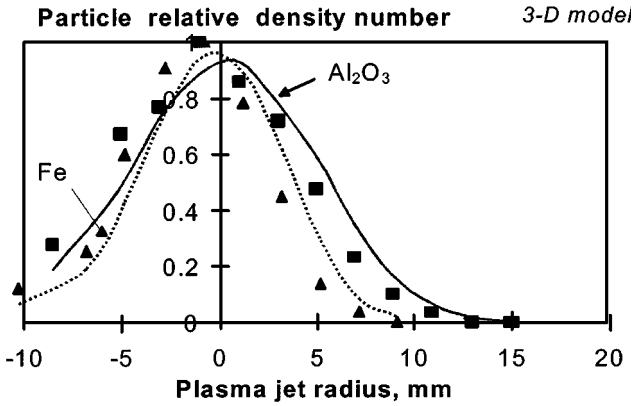

Fig. 6 Distribution of particle number vs vertical distance when alumina and iron powders are injected through two diametrically opposed injectors

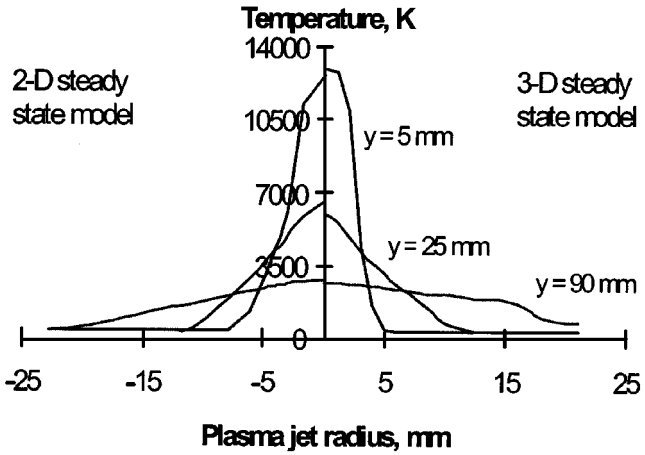

Fig. 7 Comparison of 2-D and 3-D predictions of the radial distribution of gas temperature

stronger interaction between particles and plasma jet helps to disperse the iron particles so that there is no segregation by particle size.

4.4 Comparison between 2-D and 3-D Computations

There is a reasonable agreement between the 2-D and 3-D profiles, even if the lateral spread of heat is a little faster with the 2-D model (Fig. 7).

5. Conclusions

The 2-D and 3-D computational fluid dynamics techniques have been applied to analyze the jet flow and particle behavior for the plasma co-spraying of a metal and a ceramic powder.

The 3-D modeling of the steady-state plasma process predicts reasonable particle history in the jet and distribution of both powders on the substrate. It makes it possible to take into account the effect of the carrier gas flow rate and the lateral injection of powders. Such a model can help to determine the particle size distribution and the conditions of powder injection so that the particle spray jets of the metal and ceramic powders coincide on the same spot on the target surface.

References

1. W. Smith, T.J. Jewett, S. Sampath, C C. Berndt, H. Herman, J. Fincke, and R.N. Wright: *Thermal Spray: Practical Solutions for Engineering Problems*. C. C. Berndt, ed., ASM International, Materials Park, OH, 1996, pp. 317-24.
2. M. Leylavergne, A. Vardelle, B. Dussoubs, and N. Goubot: *J. Thermal Spray Technol.*, 1998, vol. 7 (4), pp. 527-36.
3. J.D. Mattei and O. Simonin: *Logiciel ESTET, Manuel Théorique de la Version 3.1*, EDF Report HE 44/92.38B, 1992 (in French).
4. B.E. Launder and B.I. Sharma: *Lett. Heat Mass Transfer*, 1974, vol. 1, pp. 131-38.
5. M.I. Boulos, P. Fauchais, and E. Pfender: *Thermal Plasmas, Fundamental and Applications*, Plenum Press, New York, NY, 1995, vol. 1.
6. C.H. Chang and J.D. Ramshaw: *Plasma Chem. Plasma Processing*, 1993, vol. 13 (2), pp. 189-209.
7. B. Dussoubs: Ph.D. Thesis, University of Limoges, Limoges, France, 1998, 23-1998.
8. J. Pozorski and J.P. Minier: *Lagrangian Modeling of Turbulent Flows*, EDF Report HE 44/94.106, 1994.
9. M. Vardelle, A. Vardelle, P. Fauchais, and M.I. Boulos: *AIChE J.*, 1983, vol. 29 (2), 1983, pp. 236-43.
10. E. Pfender and Y.C. Lee: *Plasma Chem. Plasma Processing*, 1985, vol. 5 (3), pp. 211-37.
11. Y.C. Lee, Y.P. Chyou, and E. Pfender: *Plasma Chem. Plasma Processing*, 1985, vol. 5 (4), pp. 391-409.
12. G.T. Csanady: *J. Atm. Sci.*, 1963, vol. 20, pp. 201-08.
13. A. Papoulis: *Probability, Random Variables and Stochastic Processes*, McGraw-Hill, New York, NY, 1965.
14. S.B. Pope: *Progr. Energy Combust. Sci.*, 1985, vol. 11, pp. 119-92.
15. T. Yoshida: Ph.D. Thesis, University of Tokyo, Tokyo, 1976.
16. M. Vardelle, A. Vardelle, P. Fauchais, B. Dussoubs, T.J. Roemer, R.A. Neiser, and M.F. Smith: *Thermal Spray: Meeting the Challenges of the 21st Century*, C. Coddet, ed., ASM International, Materials Park, OH, 1998, pp. 887-94.
17. B. Dussoubs, A. Vardelle, M. Vardelle, P. Fauchais, and N. J. Themelis: *Proc. 13th Int. Symp. on Plasma Chemistry, Beijing, Aug. 18-22, 1997*, C. K. Wu, ed., Beijing University Press, Beijing, 1997, pp. 2056-61.